

# Galaxy Formation from a Low-Spin Density Perturbation in a CDM Universe

Daisuke KAWATA

*Astronomical Institute, Tohoku University, Sendai, Miyagi 980-8578*

*E-mail(DK): kawata@astr.tohoku.ac.jp*

(Received ; accepted )

## Abstract

In order to understand the formation process of elliptical galaxies which are not rotationally supported, we have carried out numerical simulations of the galaxy formation from the density perturbation with a rotation corresponding to a small spin parameter. The three-dimensional TREE N-Body/SPH simulation code used in this paper includes the dark matter and gas dynamics, radiative cooling, star formation, supernova feedback, and metal enrichment. The initial condition is a slowly rotating, top-hat over-dense sphere on which the perturbations expected in a cold dark matter (CDM) universe are superposed. By means of the stellar population synthesis, we calculated the surface brightness profile, the metallicity distribution, and the photometric properties of the end-product, and found that these properties quantitatively agree with the observed properties of bright elliptical galaxies. Thus, we conclude that, in a CDM universe, the proto-galaxy which has a spin-parameter as small as 0.02 evolves into an elliptical galaxy.

**Key words:** Galaxies: formation — Galaxies: elliptical — Numerical methods

## 1. Introduction

The new generation of large ground-based telescopes and the Hubble Space Telescope allow us to observe structures and properties of galaxies in unprecedented detail. In order to clarify the history of galaxy formation and evolution based on the observed features of galaxies, the numerical simulations are required which can be compared with these observations directly. The numerical models of galaxy formation have progressed greatly since it was first developed by a series of Larson's papers. Larson (1969) modeled the gas dissipation and the chemical evolution in galaxy formation and reproduced main properties of the observed elliptical (Larson 1974a, 1974b, 1975) and disk (Larson 1976) galaxies successfully. However, he did not take into account the details of the hydrodynamics and dissipation of the gas, and only considered the axisymmetric system. Carlberg (1984a, 1984b) and Carlberg et al. (1986) simulated the dissipational formation of spheroidal galaxies using N-body model. They succeeded in reproducing elliptical galaxies with a de Vaucouleurs surface density profile. Although they improved Larson's approach, some problems still remained. For instance, the treatment of the gas component and of the star formation process was phenomenological, because they introduced various parameters, such as the collision rate of the clouds, the rates of dissipation and star formation after encounter between gas particles, and the strength of the kinetic feedback to the surround-

ing gas caused by supernovae of new born stars. Furthermore, their simulations were performed in dimensionless units, so that there was no physically convincing way of scaling their results of simulations to dimensional units and comparing them with the observational data.

Katz & Gunn (1991) presented the modeling galaxy formation using the general-purpose code for evolving self-gravitating fluids in three dimensions, called TreeSPH (Hernquist, Katz 1989; Katz et al. 1996). TreeSPH is a fully Lagrangian code to combine smoothed particle hydrodynamics (SPH; Lucy 1977; Gingold, Monaghan 1977) with a hierarchical tree algorithm for computations of gravitational forces (Barnes, Hut 1986). Since in this method the thermodynamic state of the gas can be calculated, the dissipational effects of the gas are included as the radiative cooling following the standard cooling curves. Thus, simulations based on this numerical model can lead to physical values which can be compared with the observational data quantitatively. Furthermore, the TreeSPH simulation was presented which includes the process of the star formation (Katz 1992) and of metal enrichment due to supernova (Steinmetz, Müller 1994, 1995).

Using these numerical model, they (Katz, Gunn 1992; Katz 1992; Steinmetz, Müller 1994, 1995) investigated the collapse of an isolated constant-density perturbation which initially follows a Hubble-flow expansion and has a solid-body rotation, since external tidal fields are not included. The top-hat density perturbation consisted

of dark and baryonic matter, and included small scale perturbations assuming power spectrum index  $-2.5$ . In their model, the amount of initial solid-body rotation was specified by the dimensionless spin parameter,  $\lambda$  (Peebles 1971). They studied only the case with  $\lambda = 0.08$ , and seemed to succeed in forming a system which had some similar properties to an observed disk galaxy. However, some groups (e.g., Barnes, Efstathiou 1987; Warren et al. 1992) concluded that the spin parameter of a virialized dark matter in a cold dark matter (CDM) universe falls on a range of  $0.02 - 0.11$  with the median value of  $0.05$ . The recent analytical studies also derived the distribution of spin parameter with the similar spread and median value (e.g., Steinmetz, Bartelmann 1995; Eisenstein, Loeb 1995), in which  $\lambda = 0.08$  is near a high end value. By this reason, it is worth while investigating the properties of the system formed from the initial density perturbation with a small value of  $\lambda$ .

Therefore, we calculate the dynamical and chemical evolution of density perturbations with the small spin parameter,  $\lambda = 0.02$ . The present simulation follows a semi-cosmological manner (Katz, Gunn 1991) in order to specify initial density and velocity fields, and adopts the method of numerical simulation used by Katz (1992) and Steinmetz & Müller (1994, 1995). Using stellar population synthesis (Kodama, Arimoto 1997), we can directly compare the results of simulations with the observed properties of galaxies, such as the surface brightness profile, the half-light radius, the metallicity gradient, and the color gradient.

According to Heavens & Peacock's (1988) analytical estimation, high density peak tends to have a small value of  $\lambda$ . This reason is that higher peaks have a shorter collapse time; thus they have less time to get spun up by the environmental tidal force. On the other hand, bright elliptical galaxy is considered as the system which collapsed at high redshift and has a small rotation. It is a natural supposition that ellipticals were formed from a high density peak (e.g., Blumenthal et al. 1984). Hence, we focus on comparison the results of numerical simulation with the observed properties of elliptical galaxies.

Section 2 presents the method of numerical simulations, and the details of the top-hat model of galaxy formation are described in section 3. Section 4 presents the results of numerical simulations. Summary and discussion are described in section 5.

## 2. The Code

In our numerical simulation, the dynamics of the dark matter and stars is calculated by N-body scheme, and the gas component is modeled using the SPH. The code also includes the processes of the gas cooling and of the star formation. Many authors (e.g., Hernquist, Katz 1989; Navarro, White 1993; Katz et al. 1996; Steinmetz 1996;

Carraro et al. 1998) have already described the details of numerical model for galaxy formation which employs the SPH method. Our code is based on these previous modelings essentially and is the revised version of the SPH code in Kawata, Hanami (1998) for the application to galaxy formation. We describe details of our SPH code and the model of the cooling and star formation in the following.

### 2.1. The SPH Code

In the SPH method, the densities and other local quantities in the gas component are computed by a kernel estimation. We employ a spherically symmetric spline kernel (Steinmetz 1996),

$$W(r, h) = \frac{8}{\pi h^3} \begin{cases} 1 - 6(r/h)^2 + 6(r/h)^3 & \text{if } 0 \leq r/h \leq 1/2, \\ 2[1 - (r/h)]^3 & \text{if } 1/2 \leq r/h \leq 1, \\ 0 & \text{otherwise.} \end{cases} \quad (1)$$

Each particle has its own smoothing length,  $h_i$ , chosen so that a fixed number of neighbor particles are contained within its smoothing length (e.g., Hernquist, Katz 1989). Using this kernel, the smoothed density associated with the  $i$ -th particle is given by

$$\rho_i = \sum_j m_j W(r_{ij}, h_{ij}), \quad (2)$$

where  $r_{ij} \equiv |\mathbf{x}_i - \mathbf{x}_j|$  and  $h_{ij} = (h_i + h_j)/2$  is the pair-averaged smoothing length.

The acceleration of the  $i$ -th particle is determined by Euler's equation,

$$\frac{d\mathbf{v}_i}{dt} = -\frac{1}{\rho_i} \nabla_i (P + P_{\text{visc}}) - \nabla_i \Phi, \quad (3)$$

where  $\Phi$ ,  $P$ , and  $P_{\text{visc}}$  are the gravitational potential, the pressure, and the artificial viscous pressure, respectively. The pressure-gradient term can be written as (e.g., Steinmetz 1996)

$$\frac{1}{\rho_i} \nabla_i (P + P_{\text{visc}}) = \sum_j m_j \left( \frac{P_j}{\rho_j^2} + \frac{P_j}{\rho_j^2} + Q_{ij} \right) \nabla_i W(\mathbf{x}_{ij}, h_{ij}), \quad (4)$$

where

$$Q_{ij} = \begin{cases} \frac{-\alpha v_{s,ij} \mu_{ij} + \beta \mu_{ij}^2}{\rho_{ij}} & \text{if } \mathbf{x}_{ij} \cdot \mathbf{v}_{ij} < 0, \\ 0 & \text{otherwise,} \end{cases} \quad (5)$$

with

$$\mu_{ij} = \frac{0.5 h_{ij} \mathbf{v}_{ij} \cdot \mathbf{x}_{ij}}{r_{ij}^2 + \eta^2}. \quad (6)$$

Here, we define  $\mathbf{x}_{ij} \equiv \mathbf{x}_i - \mathbf{x}_j$  and  $\mathbf{v}_{ij} \equiv \mathbf{v}_i - \mathbf{v}_j$ . In this paper, we chose parameters  $(\alpha, \beta) = (0.5, 1.0)$  in equation (5) and  $\eta = 0.05 h_{ij}$  in equation (6) so that

the features of the one-dimensional shock tube can be well reproduced. We use the corrected artificial viscosity, which was proposed by Navarro & Steinmetz (1997):

$$\begin{aligned}\tilde{Q}_{ij} &= Q_{ij} \frac{f_i + f_j}{2}, \\ f_i &= \frac{|\langle \nabla \cdot \mathbf{v} \rangle_i|}{|\langle \nabla \cdot \mathbf{v} \rangle_i| + |\langle \nabla \times \mathbf{v} \rangle_i| + 0.0002 v_{s,i}/h_i},\end{aligned}\quad (7)$$

where  $v_s$  is the sound velocity. The velocity divergence,  $\langle \nabla \cdot \mathbf{v} \rangle_i$ , and rotation,  $\langle \nabla \times \mathbf{v} \rangle_{i,x}$ , of the  $i$ -th particle are calculated by

$$\langle \nabla \cdot \mathbf{v} \rangle_i = -\frac{1}{\rho_i} \sum_j m_j \mathbf{v}_{ij} \cdot \nabla_i W(\mathbf{x}_{ij}, h_{ij}), \quad (8)$$

$$\begin{aligned}\langle \nabla \times \mathbf{v} \rangle_{i,x} &= -\frac{1}{\rho_i} \sum_j m_j \\ &\times [v_{ij,z} \nabla_{i,y} W(\mathbf{x}_{ij}, h_{ij}) - v_{ij,y} \nabla_{i,z} W(\mathbf{x}_{ij}, h_{ij})],\end{aligned}\quad (9)$$

where  $v_{ij,x} \equiv v_{i,x} - v_{j,x}$ . The gravitational-force term of the  $i$ -th particle is the summation of the contributions from dark matter, gas, and star particles,

$$\nabla_i \Phi = -G \sum_j \frac{m_j \mathbf{x}_{ij}}{(r_{ij}^2 + \varepsilon_{ij}^2)^{3/2}}, \quad (10)$$

where  $\varepsilon_{ij} \equiv (\varepsilon_i + \varepsilon_j)/2$  is the mean softening length of  $i$  and  $j$ -th particles. The gravitational force for each particle is computed using the tree method (e.g., Barnes, Hut 1986; Pealzner, Gibbon 1996) with expansions to the quadrupole order and the tolerance parameter  $\theta = 0.8$ .

The evolution of the internal energy,  $u_i$ , of the  $i$ -th particle is determined by the energy equation (e.g., Steinmetz 1996),

$$\begin{aligned}\frac{du_i}{dt} &= \frac{P_i}{\rho_i} \sum_j m_j \mathbf{v}_{ij} \cdot \nabla_i W(\mathbf{x}_{ij}, h_{ij}) \\ &+ \frac{1}{2} \sum_j m_j Q_{ij} \mathbf{v}_{ij} \cdot \nabla_i W(\mathbf{x}_{ij}, h_{ij}) - \frac{\Lambda_i}{\rho_i} + \mathcal{H}_i,\end{aligned}\quad (11)$$

where  $\Lambda/\rho$  and  $\mathcal{H}$  are the cooling rate and the heating rate per unit mass, respectively. In this paper, we consider the cooling which is due to the radiative process of the gas having a specified metallicity and the heating which is caused by the feedback of the massive stars (see following sections for detail). The pressure,  $P$ , of each particle can be obtained by the equation of state for an ideal gas,

$$P = (\gamma - 1)\rho u, \quad (12)$$

where  $\gamma = 5/3$  for a mono-atomic gas.

The evolution of the smoothing length,  $h$ , is determined so that each particle has a roughly constant number of neighbors, i.e., the particles located within  $h$  from that particle. Thus, the smoothing length,  $h^{n+1}$ , at a time step  $n + 1$  is determined by the smoothing length,  $h^n$ , and the number of neighbors,  $N^n$ , at the previous time step  $n$ ;

$$h^{n+1} = h^n \frac{1}{2} \left[ 1 + \left( \frac{N_s}{N^n} \right)^{1/3} \right], \quad (13)$$

where  $N_s$  is a parameter (Hernquist, Katz, 1989). Our one-dimensional shock-tube tests have revealed that the acceptable range of  $N_s$  is [34, 68] in the three dimensional space. In this paper, we adopt  $N_s = 40$ .

In order to update the velocity and the position of each particle, equation (3) is integrated using a leap-frog algorithm with individual time steps (Hernquist, Katz 1989; Makino 1991). The time step of the  $i$ -th particle is chosen to be  $\Delta t_i = \min(0.3\Delta t_{\text{CFL},i}, 0.1\Delta t_{f,i})$ , where  $\Delta t_{\text{CFL}}$  is determined by the Courant–Friedrichs–Lewy condition as

$$\Delta t_{\text{CFL},i} = \frac{0.5h_i}{v_{s,i} + 1.2(\alpha v_{s,i} + \beta \max_j |\mu_{ij}|)}, \quad (14)$$

and  $\Delta t_f$  is determined by the requirement that the force should not change too much from one time step to the next time step, leading to the specification

$$\Delta t_{f,i} = \sqrt{\frac{h_i}{2} \left| \frac{d\mathbf{v}_i}{dt} \right|^{-1}}. \quad (15)$$

In a dense region, the smoothing length may become shorter than the softening length, requiring a very small time step. In order to avoid this, we set the lower limit of the smoothing length to be  $h_{\text{min}} = \varepsilon/2$ . For the collisionless particles which represent dark matter and stars, the time step is determined by  $\Delta t = \min[0.16(\varepsilon/v), 0.4(\varepsilon/|dv/dt|)^{1/2}]$ .

These time steps do not always satisfy the constraints from the time scale of the internal energy evolution, because the time scale of the radiative cooling can be very small. Thus, when the evolution of the internal energy of each particle is integrated, we do not use the individual time step scheme but the integration is carried out every time step which is the minimum among all the particles. Moreover, the energy equation is integrated using a semi-implicit method (Hernquist, Katz 1989). In the implementation, the radiative cooling is damped by the following equation in order to ensure numerical stability (Katz, Gunn 1991),

$$\begin{aligned}\left( \frac{du}{dt} \right)_{\text{rad}}^{\text{damped}} &= \frac{a(du/dt)_{\text{rad}}}{\sqrt{a^2 + [(du/dt)_{\text{rad}}]^2}}, \\ a &= 0.5 \frac{u}{\Delta t} + \left( \frac{du}{dt} \right)_{\text{ad}}.\end{aligned}\quad (16)$$

Here,  $(du/dt)_{\text{ad}}$  is the change in the thermal energy due to the adiabatic compression or expansion of the gas excluding the contribution from the undamped radiative cooling,  $(du/dt)_{\text{rad}}$ .

Our code has been vectorized and parallelized using the method of Makino (1990). The parallelization is done only in calculating gravitational forces and searching neighbors. Since these calculations occupy most of the computational time, this parallelization is very beneficial. The MPI library allows our code to run on any

computers from the serial to the parallel one, and we can obtain the same results on different computers.

## 2.2. The Radiative Cooling

We employ the cooling model in Theis et al. (1992) who approximated the cooling rate calculated by Dalgarno & McCray (1972) and Böhringer & Hensler (1989) as follows;

$$\Lambda(T, Z, n_{\text{H}}) = \Lambda_0(Z) T^{m(Z)} n_{\text{H}}^2 \text{ erg cm}^{-3} \text{ s}^{-1}, \quad (17)$$

where  $Z$  and  $n_{\text{H}}$  are the metallicity and the hydrogen number density of the gas, respectively.  $\Lambda_0(Z)$  and  $m(Z)$  are defined for different temperature ranges as follows; at  $10^4 \text{ K} \leq T < 10^5 \text{ K}$ ,

$$\begin{aligned} m(Z) &= 30Z, \\ \Lambda_0(Z) &= 4 \times 10^{-22.1-4m(Z)}, \end{aligned}$$

at  $T \geq 10^5 \text{ K}$ ,

$$\begin{aligned} m(Z) &= \frac{2.5 + 7\sqrt{Z}}{5 - \log(1.48 \times 10^{11} Z^{1.1} + 10^6)}, \\ \Lambda_0(Z) &= 10^{-22.1-5m(Z)+7\sqrt{Z}}. \end{aligned}$$

For temperatures above  $5 \times 10^4 \text{ K}$ , bremsstrahlung becomes important, which is expressed here as:

$$\Lambda_{\text{br}} = 1.4 \times 10^{-27} (f^{\text{ion}})^2 n_{\text{e}} n_{\text{ion}} T^{0.5} \langle g_{\text{ff}} \rangle, \quad (18)$$

where  $\langle g_{\text{ff}} \rangle \approx 1.35$  is an averaged Gaunt factor and,

$$\begin{aligned} f^{\text{ion}} &= n_{\text{e}}/n_{\text{ion}}, \\ n_{\text{ion}} &= \frac{n_{\text{H}}}{1 - Y - Z} \left( 1 - \frac{3}{4}Y - \frac{17}{18}Z \right), \\ n_{\text{e}} &= \frac{n_{\text{H}}}{1 - Y - Z} \left( 1 - \frac{1}{2}Y - \frac{7}{9}Z \right). \end{aligned}$$

Here,  $Y$  denotes the mass fraction of helium and we set  $Y = 0.24$ . We do not consider the cooling below  $10^4 \text{ K}$ , because our simulation does not have enough mass resolution for cooling processes in such low temperatures (e.g.,  $\text{H}_2$  cooling) and because the cooling rate declines rapidly below  $10^4 \text{ K}$ . Furthermore, the heat sources such as the UV background radiation, which are ignored in this paper, could warm the gas components to this temperature easily. Thus, we set the lower limit of the temperature to be  $T_{\text{lim}} = 10^4 \text{ K}$  (Katz, Gunn 1991).

## 2.3. The Star Formation

We model the star formation using a method similar to that of Katz (1992) and Katz et al. (1996). We assume that the star formation occurs where the gas density is larger than a critical density,  $\rho_{\text{crit}} = 7 \times 10^{-26} \text{ g cm}^{-3}$ , and where the gas velocity field is convergent,  $\nabla \cdot \mathbf{v}_i <$

0. When a gas particle is eligible to form stars, its star formation rate (SFR) is,

$$\frac{d\rho_*}{dt} = -\frac{d\rho_g}{dt} = \frac{c_* \rho_g}{t_g}, \quad (19)$$

where  $c_*$  is a dimensionless SFR parameter and  $t_g = \sqrt{3\pi/16G\rho_g}$  is the dynamical time, which is longer than the cooling time scale in the region eligible to form stars. This formula corresponds to the Schmidt law that SFR is proportional to  $\rho_g^{1.5}$ . In this paper, we set  $c_* = 1$ . Equation (19) implies that the probability,  $p_*$ , which one gas particle forms stars during a discrete time step,  $\Delta t$ , is

$$p_* = 1 - \exp(-c_* \Delta t / t_g). \quad (20)$$

In order to avoid making an intolerably large number of new star particles with different masses, we set the whole gas particle transforming to one star particle with this probability. After the particle changed to the star, it behaves as a collisionless particle dynamically.

We take into account the energy feedback to the surrounding gas by supernovae. We assume that each supernova yields thermal energy of  $10^{51}$  ergs. For simplification, we assume that each massive star ( $> 8M_{\odot}$ ) explodes within the simulation time step in which it was born (instantaneous recycling). In our simulation, the feedback also adds the ejected mass to the surrounding gas. In this process, a portion of metals produced in the stars is also returned to the gas, leading to chemical enrichment. We assume that an  $m M_{\odot}$  star yields  $(0.357m - 2.2) M_{\odot}$  of metal (Maeder 1987; Steinmetz, Müller 1994). The ejected mass is  $(m - 1.4) M_{\odot}$ , where the remnant mass is assumed to be  $1.4 M_{\odot}$ . The feedback energy,  $E_{\text{SN}}$ , the ejected mass,  $M_{\text{SN}}$ , and the ejected metals,  $M_{\text{ZSN}}$ , can be obtained from the Salpeter IMF ( $x = 1.35$ ) with the lower mass limit of  $0.1 M_{\odot}$  and the upper mass limit of  $60 M_{\odot}$ . This IMF leads to  $M_{\text{SN}} \sim 0.122 M_{\odot}$ ,  $E_{\text{SN}} \sim 0.007310 \times 10^{51}$  ergs, and  $M_{\text{ZSN}} \sim 0.02754 M_{\odot}$ , for each  $1 M_{\odot}$  star born. These mass, energy, and metals are smoothed over the neighbor particles using the SPH smoothing algorithm. For example, when the  $i$ -th particle changes from the gas to a star, the increment of the mass of the  $j$ -th neighbor particle due to explosion of the new star is given by

$$\Delta M_{\text{SN},j} = \frac{m_j}{\rho_{g,i}} M_{\text{SN},i}, \quad (21)$$

where

$$\rho_{g,i} = \langle \rho_g(\mathbf{x}_i) \rangle = \sum_{j \neq i} m_j W(r_{ij}, h_{ij}). \quad (22)$$

## 3. The Model

Using the above code, we calculate a semi-cosmological model as follows. We consider an isolated sphere

on which small-scale fluctuations corresponding to a CDM power spectrum are superimposed. Here, we use Bertschinger's software COSMICS (Bertschinger 1995) in generating initial fluctuations. To incorporate the effects of fluctuations with longer wavelengths, the density of the sphere has been enhanced and a rigid rotation corresponding to a spin parameter,  $\lambda$ , has been added. The initial condition of this model is determined by four parameters  $\lambda$ ,  $M_{\text{tot}}$ ,  $\sigma_{8,\text{in}}$ , and  $z_c$ : the spin parameter is defined by

$$\lambda \equiv \frac{J|E|^{1/2}}{GM_{\text{tot}}^{5/2}}, \quad (23)$$

where  $J$  is the total angular momentum of the system,  $E$  is the binding energy when the system turns around, and  $M_{\text{tot}}$  is the total mass of this sphere, which is composed of dark matter and gas;  $\sigma_{8,\text{in}}$  is an rms mass fluctuation in a sphere of radius  $8 h^{-1}$  Mpc, which normalizes the amplitude of the CDM power spectrum;  $z_c$  is the expected collapse redshift. If the top-hat density perturbation has an amplitude of  $\delta_i$  at the initial redshift,  $z_i$ , we have  $z_c = 0.36\delta_i(1+z_i) - 1$  (e.g., Padmanabhan 1993). Thus, when  $z_c$  is given,  $\delta_i$  at  $z_i$  is determined.

Our simulations assume a flat universe ( $\Omega = 1$ ) with a baryon fraction of  $\Omega_b = 0.1$  and a Hubble constant of  $H_0 = 50 \text{ km s}^{-1} \text{ Mpc}^{-1}$ . In this paper, we focus on the evolution of a top-hat density perturbation with a spin parameter  $\lambda = 0.02$ . This is close to the minimum value of the spin parameter possible in a CDM universe, according to the results of the N-body simulation (Barnes, Efstathiou 1987; Warren et al. 1992). Other parameters are  $M_{\text{tot}} = 8 \times 10^{11} M_{\odot}$ ,  $\sigma_{8,\text{in}} = 0.5$ , and  $z_c = 2$ . Then, the radius of the proto-galactic sphere is 32.17 kpc (in real space) at the initial redshift of  $z_i = 40$ .

We carry out two simulations with the different numbers of particles,  $N_p$ . One simulation has  $N_p = 9171$  (Model 1) and another has  $N_p = 3071$  (Model 2). In Model 1, the initial redshift is set to be  $z_i = 40$ , while in Model 2,  $z_i = 25$ . The numerical simulation should start from a redshift at which small scale perturbations are weak enough. The simulation with large  $N_p$  can include smaller-scale perturbations than that with small  $N_p$ , and the perturbations on a smaller scale have a larger amplitude than large-scale perturbations in the CDM power spectrum. This is why the initial redshift of Model 1 is taken to be higher. In Model 1 (Model 2), the masses of gas, star, and dark matter particles are  $8.72 \times 10^6$  ( $2.61 \times 10^7$ ),  $8.72 \times 10^6$  ( $2.61 \times 10^7$ ), and  $7.85 \times 10^7$  ( $2.34 \times 10^8$ )  $M_{\odot}$ , respectively, and the softening lengths of gas, star, and dark matter particles are 1.20 (1.73), 1.20 (1.73), and 2.50 (3.61) kpc, respectively.

## 4. Results

We simulate the evolution of the galaxy based on the two models from the redshift  $z_i$  to the present,  $z = 0$ . The angular momentum of the whole system is conserved with sufficient accuracy: the error is less than 0.3 (1) % in Model 1 (Model 2). Figure 1 shows the evolution of the system in Model 1. These panels show the projection of the particles to the  $x$ - $z$  plane, where we take the  $z$ -axis to be the initial rotational axis. At redshift of  $z = 4.88$ , the system is expanding with the Hubble Flow. The amplitude of the initial top-hat density perturbation is chosen so that the system should turn around at  $z = 3.71$ . At  $z = 3.54$ , small clumps are formed and star formation begins in these clumps. These clumps have merged and the whole system has collapsed at  $z = 1.89$ . The stars are formed in a burst and gas particles diminish, changing into star particles. At  $z = 0.84$ , the system has already relaxed and is evolving almost passively.

The history of the SFR is shown in figure 2. Figure 2 also shows the SFR in Model 2. In spite of the difference in the number of particles, the two simulations yielded similar results. From figure 2, we see that the major star formation begins due to the collapse of whole system and continues for about 1 Gyr with a rate of about  $50 M_{\odot} \text{ yr}^{-1}$ . At the age of universe  $t = 4$  Gyr ( $z \sim 1.2$ ), the star formation is almost quenched owing to the exhaustion of the gas.

The distribution of star particles at  $z = 0$  is shown in figure 3. Figure 3 shows the  $x$ - $y$  and  $x$ - $z$  projection. Both projections look quite similar. The final stellar system seems to be nearly spherical due to the low initial spin, in contrast to the results of Katz (1992) who made the disk system contracted along the rotational axis due to the high initial spin.

Figure 4 shows the surface mass density profile of the final stellar system at  $z = 0$  in Model 1 and Model 2. These surface densities are obtained for the cylindrical shells of various radii in the  $x$ - $y$  projection. We have confirmed that these profiles do not change in other projections. The surface density profile in figure 4 is in good agreement with the de Vaucouleurs law,

$$\Sigma = \Sigma_e \exp \left\{ -7.67 \left[ (R/R_{\text{h,m}})^{1/4} - 1 \right] \right\}, \quad (24)$$

where  $R_{\text{h,m}}$  is the radius containing half the total mass and  $\Sigma_e$  is the mass density at  $R_{\text{h,m}}$ . These parameters are summarized in table 1. Here,  $R_{\text{h,m}}$  is comparable to the softening length especially in Model 2. In order to examine the effect of the softening length of star particles,  $\varepsilon_s$ , which equals that of gas particles, we also carry out five simulations ( $N_p = 3071$ ) with the softening length  $\varepsilon_s = 0.25\varepsilon_{s,0}$ ,  $0.5\varepsilon_{s,0}$ ,  $0.75\varepsilon_{s,0}$ ,  $1.25\varepsilon_{s,0}$ , and  $1.5\varepsilon_{s,0}$ , where  $\varepsilon_{s,0} = 1.73$  kpc denotes the standard value used in Model 2. Figure 5 shows  $R_{\text{h,m}}$  at  $z = 0$  as a function of  $\varepsilon_s$ . It is clear that  $\varepsilon_{s,0}$  is an appropriate value, because  $R_{\text{h,m}}$

Fig. 1. Time evolution of the system in Model 1. The upper, middle, and lower panels show the distributions of the dark matter, the gas, and the stars, respectively. Each panel measures 200 kpc across and shows the  $x$ - $z$  projection of the particles, where we set the  $z$ -axis to be the initial rotational axis.

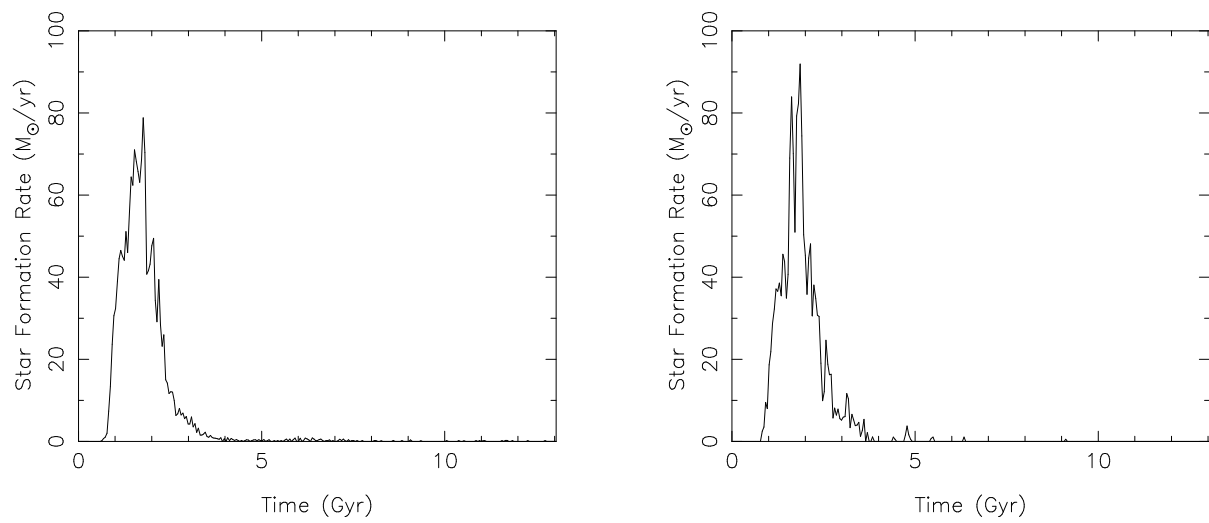


Fig. 2. Star formation rate in  $M_{\odot} \text{ yr}^{-1}$  as a function of the age of universe in Model 1 (left) and Model 2 (right), respectively.

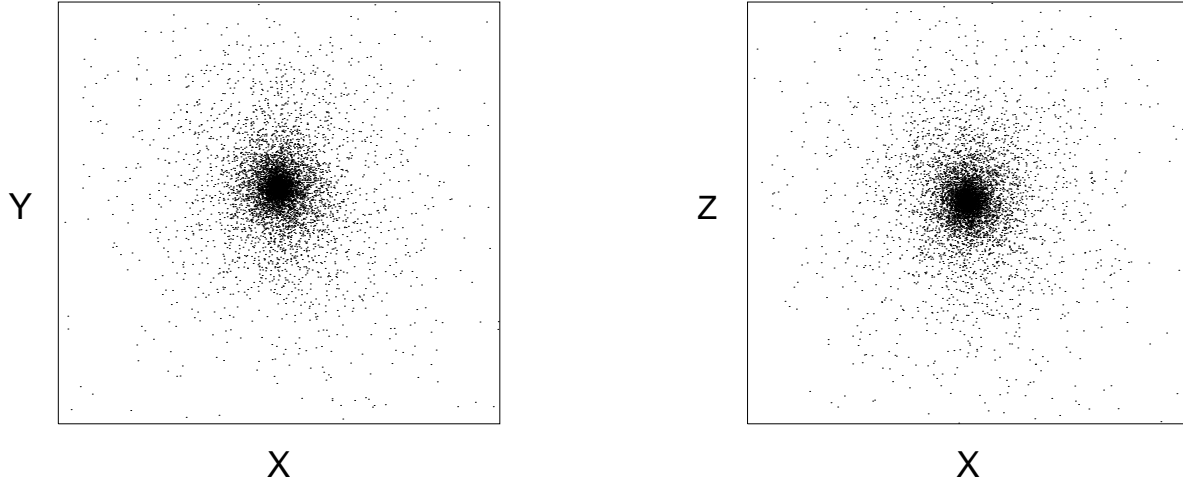


Fig. 3. The particle distribution of stars at  $z = 0$ . The left (right) panel shows the  $x$ - $y$  ( $x$ - $z$ ) projection, where the  $z$ -axis is the initial rotational axis. Each panel measures 100 kpc across.

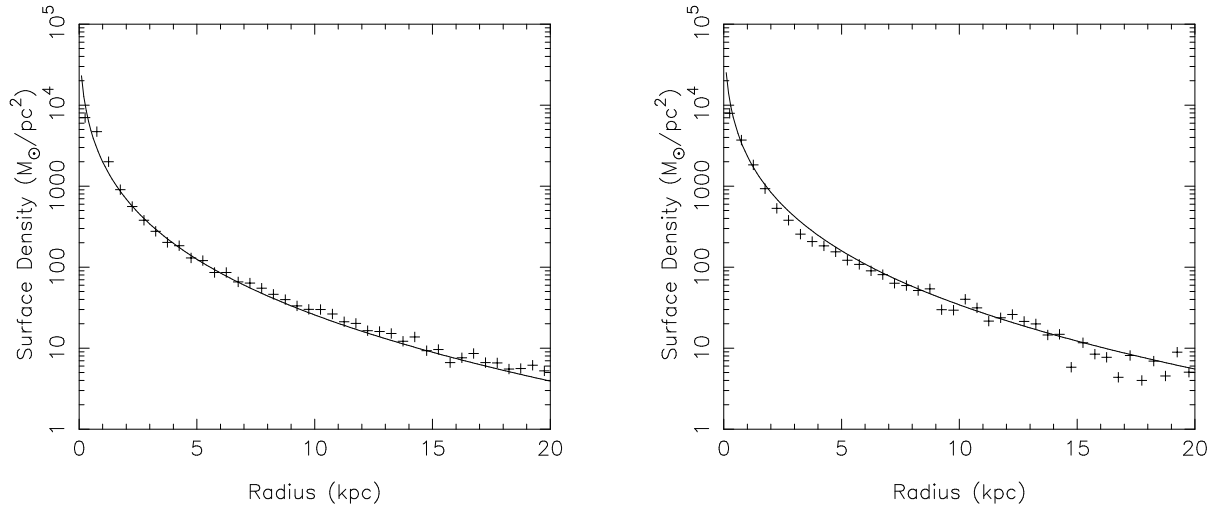


Fig. 4. The surface mass density profiles in Model 1 (left) and Model 2 (right), respectively. The solid line shows the de Vaucouleurs law given by equation (24) with parameters being listed in table 1.

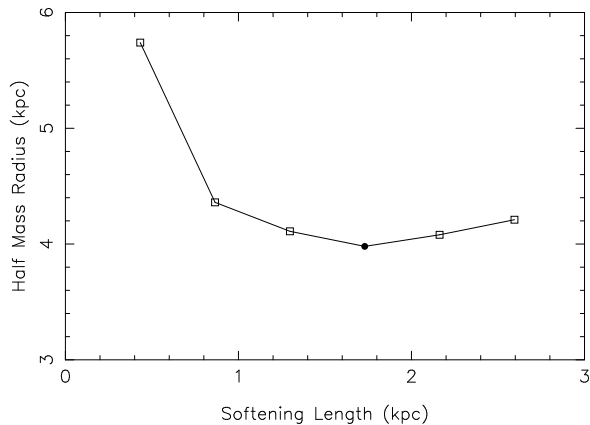


Fig. 5. Half-mass radius as a function of the softening length of the star particles in the simulations with  $N_p = 3071$ . A filled circle corresponds to the softening length in Model 2 ( $\varepsilon_{s,0} = 1.73$  kpc).

does not depend on the softening length around  $\varepsilon_{s,0}$ . It is worth noting that, in the range  $\varepsilon_s < 0.5\varepsilon_{s,0}$ , the softening length is so small that the artificial two-body relaxation causes the rise of  $R_{h,m}$ . Figure 6 shows this effect clearly. In the case  $\varepsilon_s = \varepsilon_{s,0}$ ,  $R_{h,m}$  does not change from  $z = 0.58$ , at which the system has already relaxed, to the present epoch  $z = 0$ . In the case  $\varepsilon_s = 0.25\varepsilon_{s,0}$ , however, the central concentration is diluted and  $R_{h,m}$  goes up at  $z = 0$ . Thus, the resulting value of  $R_{h,m}$  appears to be trustful only over a limited range of  $\varepsilon_s$ , which includes  $\varepsilon_{s,0}$  adopted in Model 2.

It is known that a violent relaxation for sufficiently deep central potentials reproduces the de Vaucouleurs law (Hjorth, Madsen 1991 and references therein). The deep potential causes the strong scattering which tightly bound particles experience near the center, and leads to the outer envelope of the de Vaucouleurs profile. In dissipationless collapse, a cold collapse is preferred to yield a deep enough central potential (e.g., van Albada 1982). However, the dissipation is a crucial component of galaxy formation. Carlberg et al. (1986) found that dissipation, leading to a deep central potential, could help get a good

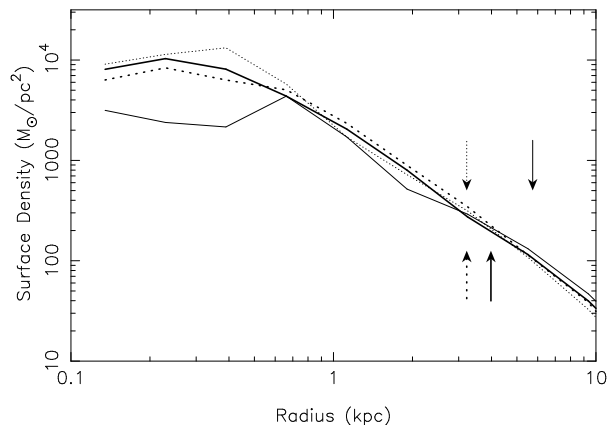


Fig. 6. The surface mass density profiles at  $z = 0.58$  (short-dashed lines) and at  $z = 0$  (solid lines), respectively. The thick and normal lines correspond to the case of  $\varepsilon_s = \varepsilon_{s,0}$  and the case of  $\varepsilon_s = 0.25\varepsilon_{s,0}$ , respectively. The arrows indicate the position of the half-mass radius.



de Vaucouleurs profile. We can infer that our numerical simulations also result in the de Vaucouleurs profile owing to the collapse combined with the dissipation.

In Model 1, we analyze the kinematic properties, the rotation velocity and the velocity dispersion. The maximum rotation velocity,  $V_m$ , is 25 km/s at the radius of 9 kpc where the rotation curve flattens out, and the mean velocity dispersion,  $\bar{\sigma}$ , within the half-mass radius is 116 km/s.  $V_m/\bar{\sigma}$  is an important value characterizing the kinematic properties of elliptical galaxies.  $V_m/\bar{\sigma} = 0.2$  means that this system is slowly rotating and supported by the velocity dispersion due to the low initial spin. This value resembles that of bright elliptical galaxies (e.g., Davies et al. 1983).

Our simulation includes the chemical evolution process. As a result, each star particle has its own age and metallicity. From this information, we can obtain the SED (Spectral Energy Distribution) using the SSPs (Single Stellar Populations) in Kodama, Arimoto (1997). Consequently, we can analyze distributions of the luminosity and color. Figure 7 shows the surface brightness ( $L_{\odot, V} \text{ pc}^{-2}$ ) in  $V$  band as a function of the radius in Model 1 and Model 2. The surface brightness profile also matches the de Vaucouleurs law very well, using the half-light radius  $R_{h,1}$  and the luminosity  $I_e$  at  $R_{h,1}$  given in table 1.

Based on the luminosity of each star particle, we also obtain the radial profile of the metallicity and color weighted by the luminosity. Figure 8 shows the projected metallicity and the  $V - K$  color profile in Model 1. The metallicity has a gradient of  $\Delta \log Z / \Delta \log r \sim -0.3$ , which is consistent with the value  $\Delta \log Z / \Delta \log r = -0.2 \pm 0.1$  observed by Davies et al. (1993). The  $V - K$  color also has a similar amount of gradient which is caused mainly by the spatial change of metallicity.

In table 1, we summarize the photometric properties of this stellar system at  $z = 0$ . The eighth column in table 1 gives the  $V - K$  color within a 10 kpc aperture, which is the same aperture as adopted in the observation by Bower et al. (1992), who investigated the color-magnitude relation of early-type galaxies in the Coma and Virgo clusters. The half-light radius, the metallicity gradient, and the  $V - K$  color obtained in the simulation agree with those values observed for a  $M_V \sim -20$  elliptical galaxy (e.g., Faber et al. 1989; Peletier et al. 1990; Bender et al. 1992; Bower et al. 1992; Davies et al. 1993). There is no significant difference between the two simulations which have different  $N_p$ . Therefore, these simulations have a sufficiently large particle number and, hence, sufficient mass resolution to reproduce the main properties of the elliptical galaxy with enough accuracy.

## 5. Summary and Discussion

We simulated the galaxy formation from a top-hat density perturbation with a small spin parameter,  $\lambda = 0.02$ . The stellar system formed in the simulation is spherical and has a mass distribution which is in good agreement with the de Vaucouleurs law. This system was formed through turning around from the Hubble expansion and subsequent merging of small clumps originating in initial CDM density perturbations. We also obtained photometric properties by simulating star formation process which follows chemical evolution. These properties were found to be similar to the observed properties of elliptical galaxies. The results of our simulation clearly show that, in a CDM universe, the proto-galaxy which has a spin-parameter as small as 0.02 evolves into an elliptical galaxy.

Using three-dimensional SPH numerical simulation, Mori et al. (1999) investigated elliptical galaxy formation. They assumed a virialized proto-galactic gaseous cloud as the initial condition. As Katz & Gunn (1991) showed, however, the gas never gets heated to the virial temperature in the hierarchical galaxy formation which was adopted in our simulations. The present simulations thus improve on their non-cosmological simulations.

In our numerical simulation, the luminosity profile is in good agreement with the de Vaucouleurs law as well as the mass distribution, in spite of the difference between the half mass and light radii. Figure 9 shows the projected stellar mass-to-luminosity ratio in  $V$  band as a function of the radius in Model 1. Due to the metallicity gradient, the mass-to-luminosity ratio decreases as the radius increases. This gradient of mass-to-luminosity ratio leads to the half-light radius larger than the half-mass radius. However, the de Vaucouleurs law is held for the luminosity, if the mass-to-luminosity ratio varies with respect to the radius as follows,

$$\frac{\Sigma(r)}{I(r)} = \frac{\Sigma_e}{I_e} \exp \left[ -7.67 \left( R_{h,m}^{-1/4} - R_{l,m}^{-1/4} \right) r^{1/4} \right]. \quad (25)$$

In figure 9, the solid line corresponds to this equation with parameters of table 1. The simulation results match this line. Thus, this gradient of mass-to-luminosity ratio does not make the luminosity profile fail to reproduce the de Vaucouleurs law.

It is notable that we obtain the projected metallicity gradient which is consistent with the observed one for elliptical galaxies. This gradient is caused by different star formation history at different sites. Figure 10 shows the time variations of SFR in the regions of inside and outside the half-light radius in Model 1. It is clear that the star formation holds on longer time in the inner region than in the outer region. Since the residual gas is polluted by the past star formation, metal-rich stars are formed in the central region where the duration of the

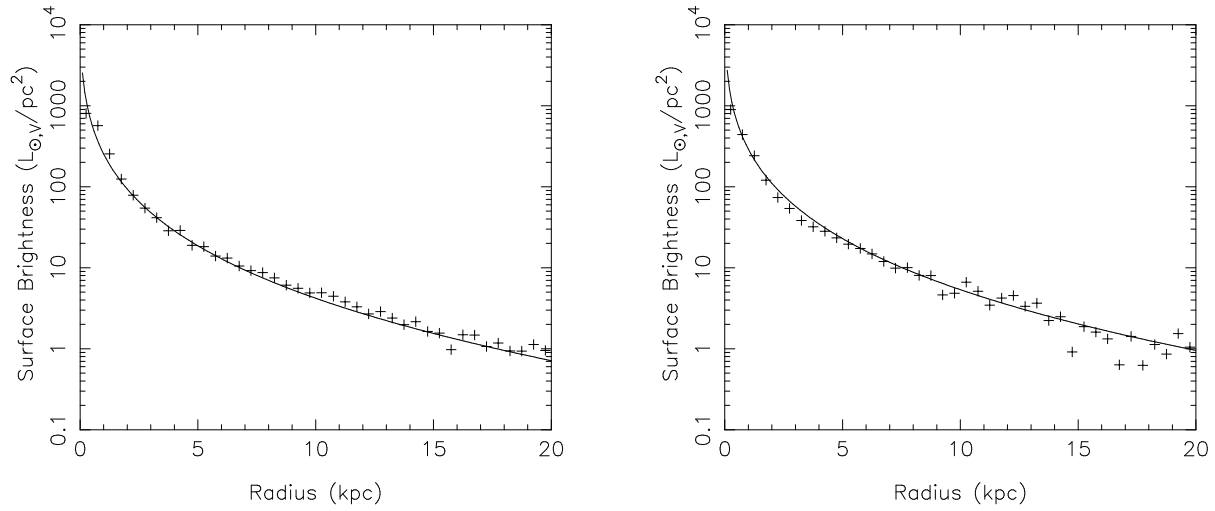


Fig. 7. The surface brightness profiles in Model 1 (left) and Model 2 (right), respectively. The solid line shows the de Vaucouleurs law with parameters being listed in table 1.

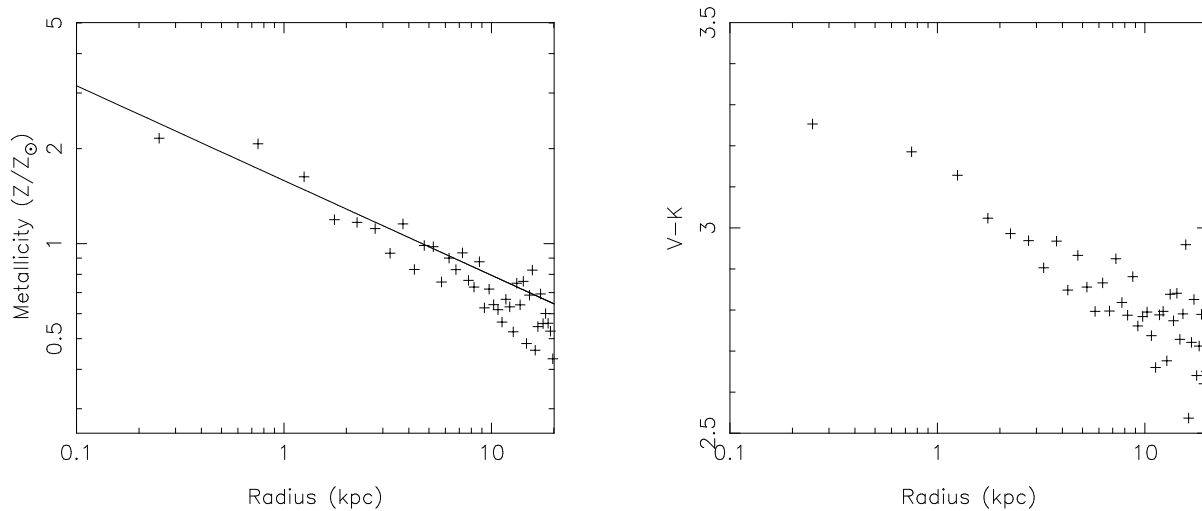


Fig. 8. The projected metallicity (left) and the  $V - K$  color (right) versus the radius in Model 1. In the left panel, the solid line has the gradient of  $\Delta \log Z / \Delta \log r = -0.3$ .

Table 1. de Vaucouleurs law parameters and photometric properties.

	$N_p$	$\Sigma_e$ ( $M_\odot \text{ pc}^{-2}$ )	$R_{h,m}$ (kpc)	$I_e$ ( $L_{\odot,V} \text{ pc}^{-2}$ )	$R_{h,l}$ (kpc)	$M_V$	$V - K$ ( $< 10\text{kpc}$ )
Model 1	9171	250	3.54	23	4.49	-20.34	3.164
Model 2	3071	250	3.99	23	4.99	-20.34	3.166

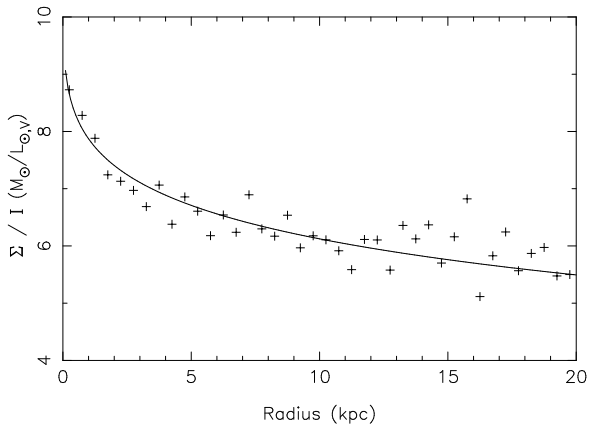


Fig. 9. The projected stellar mass-to-luminosity ratio in V band as a function of the radius in Model 1. The solid line corresponds to equation (25) with parameters of table 1.

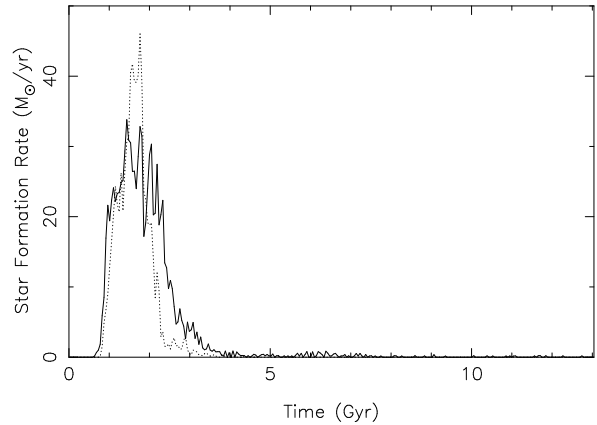


Fig. 10. The history of the star formation rate (SFR) in different regions in Model 1. The solid line is the SFR within the half-light radius, while the dotted line is that outside the half-light radius.

star formation is long.

Since the cooling of the gas overcame the feedback from massive stars, our simulations did not lead to outflow of the gas in the form of a galactic wind, which is often postulated to explain photometric properties of the elliptical galaxy population (e.g., Larson 1974b, Arimoto, Yoshii 1987). Although our numerical model ignored some important feedback processes like the stellar wind and the Type Ia supernova, the system which we simulated might be too massive to allow a galactic wind. To confirm this conjecture, we need to simulate the systems of different masses. The ultimate goal of such an extensive attempt is to reproduce the color-magnitude relation of elliptical

galaxies (e.g., Bower et al. 1992). A forthcoming paper will discuss the properties of model elliptical galaxies as a function of galaxy mass.

D.K. would like to thank M. Noguchi for valuable discussion, and the editor, S. Mineshige, for correcting the draft of this paper. D.K. also acknowledges the Astronomical Institute, Tohoku University and the Astronomical Data Analysis Center of the National Astronomical Observatory, Japan where the numerical computations presented in this paper were performed. This work was supported in part by the Japan Atomic Energy Research Institute.

## References

- Arimoto N., Yoshii Y. 1987, *A&A* 173, 23  
 Barnes J.E., Hut P. 1986, *Nature* 324, 446  
 Barnes J., Efstathiou G. 1987, *ApJ* 319, 575  
 Bender R., Burstein D., Faber S.M. 1992, *ApJ* 399, 462  
 Bertschinger E. 1995 preprint (astro-ph/9506070)  
 Blumenthal G.R., Faber S.M., Primack J.R. Rees M.J. 1984, *Nature*, 311, 517  
 Bower R.G., Lucey J.R., Ellis R.S. 1992, *MNRAS* 254, 601  
 Böhringer H., Hensler G. 1989, *A&A* 215, 147  
 Carlberg R.G. 1984a, *ApJ* 286, 403  
 Carlberg R.G. 1984b, *ApJ* 286, 416  
 Carlberg R.G., Lake G., Norman C.A. 1986, *ApJ* 300, L1  
 Carraro G., Lia C., Chiosi C. 1998, *MNRAS* 297, 1021  
 Dalgarno A., McCray R.A. 1972, *ARA&A* 10, 375  
 Davies R.L., Efstathiou G., Fall S.M., Illingworth G., Schechter P.L. 1983, *ApJ* 266, 41  
 Davies R.L., Sadler E.M., Peletier R.F. 1993, *MNRAS* 262, 650  
 Eisenstein D.J., Loeb A. 1995, *ApJ*, 439, 520  
 Faber S.M., Wegner G., Burstein D., Davies R.L., Dressler A., Lynden-Bell D., Terlevich R.J. 1989, *ApJS*, 69, 763  
 Gingold R.A., Monaghan J.J. 1977, *MNRAS* 181, 375  
 Heavens A., Peacock J. 1988, *MNRAS* 232, 339  
 Hernquist L., Katz N. 1989, *ApJS* 70, 419  
 Hjorth J., Madsen J. 1991, *MNRAS* 253, 703  
 Katz N. 1992, *ApJ* 391, 502  
 Katz N., Gunn J.E. 1991, *ApJ* 377, 365  
 Katz N., Weinberg D.H., Hernquist L. 1996, *ApJS* 105, 19  
 Kawata D., Hanami H. 1998, *PASJ* 50, 547  
 Kodama T., Arimoto N. 1997, *A&A* 320, 41  
 Larson R.B. 1969, *MNRAS* 145, 405  
 Larson R.B. 1974a, *MNRAS* 166, 585  
 Larson R.B. 1974b, *MNRAS* 169, 229  
 Larson R.B. 1975, *MNRAS* 173, 671  
 Larson R.B. 1976, *MNRAS* 176, 31  
 Lucy L.B. 1977, *AJ* 82, 1013  
 Maeder A. 1987, *A&A* 173, 247  
 Makino J. 1990, *J. Comp. Phys* 87, 148  
 Makino J. 1991, *PASJ* 43, 859  
 Mori M., Yoshii Y., Nomoto K. 1999, *ApJ* 511, 585  
 Navarro J.F., Steinmetz M. 1997, *ApJ* 478, 13  
 Navarro J.F., White S.D.M. 1993, *MNRAS* 265, 271  
 Padmanabhan T. 1993, *Structure formation in the universe* (Cambridge Univ. Press, Cambridge) ch8  
 Pealzner S., Gibbon P. 1996, *MANY-BODY TREE METHODS IN PHYSICS* (Cambridge Univ. Press, Cambridge) ch2  
 Peebles P.J.E. 1971, *A&A* 11, 377  
 Peletier R.F., Valentijn E.A., Jameson R.F. 1990, *A&A* 233, 62  
 Steinmetz M. 1996, *MNRAS* 278, 1005  
 Steinmetz M., Bartelmann M. 1995, *MNRAS* 272, 570  
 Steinmetz M., Müller E. 1994, *A&A* 281, L97  
 Steinmetz M., Müller E. 1995, *MNRAS* 276, 549  
 Theis Ch., Burkert A., Hensler G. 1992, *A&A* 265, 465  
 van Albada T.S. 1982, *MNRAS* 201, 939  
 Warren M., Quinn P.J., Salmon J.K., Zurek W.H., 1992, *ApJ* 399, 405

This figure "fig1.gif" is available in "gif" format from:

<http://arxiv.org/ps/astro-ph/9909122v1>